HIGH VELOCITY PERFORATION SIMULATIONS OF LIGHTWEIGHT TARGET PLATES USING A MODIFIED JOHNSON-COOK MODEL

S. SWADDIWUDHIPONG* and MD. JAHIDUL ISLAM†

Department of Civil and Environmental Engineering
National University of Singapore,
No. 1 Engineering Drive 2, Singapore 117576
*ceesomsa@nus.edu.sg
†jahidul_islam@nus.edu.sg

ZISHUN LIU‡

Institute of High Performance Computing, Fusionopolis Way
#16-16 Connexis, Singapore 138632
liuzs@ihpc.a-star.edu.sg

Because of their superior ballistic and mechanical properties, lightweight materials like titanium alloy Ti-6Al-4V and aluminum alloy AA5083-H116 have been frequently used for aerospace and military applications. Tests of ballistic limit velocity are limited by expensive nature of the experimental setup, and indeed, that can be resolved by adopting numerical simulations. Numerical study involving the finite element method (FEM) suffers from severe element distortion problem when used for high velocity impact analysis. Therefore, the coupled smooth particle hydrodynamics — finite element method (SFM) has been adopted to study the perforation of Ti-6Al-4V and AA5083-H116 target plates with thicknesses of 26.72 mm and 25 mm, respectively. In the SFM, smooth particle hydrodynamics (SPH) method is incorporated in the severely distorted regions and the FEM otherwise. Effects of strain rate and adiabatic heating are significant for high velocity impact problems, and hence, a constitutive model incorporating effects of high strain rate and adiabatic temperature is proposed. The constitutive model is verified and finally adopted for perforation studies. Close correlation between the numerical and experimental ballistic limit velocities are accomplished. The study shows that the proposed method is able to emulate the failure mechanisms of the target plates without any numerical problem.

Keywords: Element distortion; Finite Element Method (FEM); High velocity impact; Perforation; Smooth Particle Hydrodynamics (SPH); Titanium alloy.

‡Corresponding author.

1. Introduction

Titanium is the fourth most abundant structural element. It is known as the space-age element because of its superior mass efficiency and excellent corrosion resistance. Mass efficiency is the ratio of weight per unit area of rolled homogenous armour (RHA) steel over weight per unit area of test material. Titanium has 30–80% more mass efficiency compare to RHA [Burkins *et al.*, 2001; Montgomery and Wells, 2001]. Titanium exists in two phases namely, alpha and beta phases. The alpha phase titanium is stable up to the beta transus temperature of 882°C, beyond which and up to the melting temperature titanium exists in the beta phase [Burkins *et al.*, 1996]. Inclusion of alloying elements, like aluminum and vanadium in titanium shifts the beta transus temperature to 996°C. Ti-6Al-4V has high strength to weight ratio and toughness, and excellent resistance against corrosion, which allow it to be used in aerospace, defense and biomedical applications.

Aluminum alloys have excellent strength to weight ratio and good corrosion resistance, and hence, they are widely employed in aerospace, automobile and military industries. In particular, aluminum-magnesium alloys (AA5XXX class) which have high strength, are an excellent choice for transportation fields where light weight is desirable without compromising the structural integrity. These alloys also used for military purpose against ballistic penetrators and low temperatures [Hatch, 1984]. Aluminum-magnesium alloy AA5083-H116 is the second strongest alloy in AA5XXX class alloys [Børvik *et al.*, 2004] where temper H116 is a special strain hardening treatment with special temperature control.

Titanium and aluminum alloys are used for lightweight armors and vehicles. Threats against these protective structure subjected to projectile impact are evaluated from the ballistic perforation tests. Because of high production and fabrication cost of titanium alloys, very few studies have been performed to achieve the ballistic limit velocities for Ti-6Al-4V. Burkins *et al.* [2001] performed penetration/perforation tests of the aerospace specification MIL-T-9046J titanium alloy Ti-6Al-4V to determine the ballistic limit velocities of various plate thicknesses. However, to the author's knowledge, no numerical perforation study has been performed for Ti-6Al-4V with 'fragment-simulating projectile (FSP) at initial velocities ranging between 1000–1300 m/s. Børvik *et al.* [2004] conducted ballistic perforation tests of AA5083-H116 aluminum plates with various plate thicknesses by conical nose projectiles and reported that ballistic limit velocities increase with increasing plate thicknesses.

Numerical methods are capable of offering solutions with greater accuracy provided that a robust discretization method along with an appropriate material model is adopted. Johnson [1977] introduced a Lagrangian finite element formulation with explicit time integration method for high velocity impact problems. Since then it has been used for wide varieties of high velocity impact problems. Although the finite element method (FEM) has several advantages over other numerical approaches, e.g. for low velocity impact problems, it have been successfully used to study dynamic

response of plate and shell structures under impact [Swaddiwudhipong and Liu, 1996; 1997; Liu and Swaddiwudhipong 1997, Liu *et al.* 2005], however for high velocity impact problem, it has a major drawback. In the presence of large deformation, it suffers from severe element distortion that could cause negative volumes for elements. Large deformation may also introduce numerical errors in the simulated result. This problem can be solved by adopting coupled smooth particle hydrodynamics-finite element method (SFM), especially for the high velocity impact simulations [Swaddiwudhipong *et al.*, 2010]. Smooth particle hydrodynamics (SPH), a mesh-free method, is capable of handling large deformation without severe element distortion problem. Although originally it was developed for astrophysics problem by Lucy [1977], and Gingold and Monaghan [1977], it has been employed for the solid mechanics problems since early 1990s [Libersky and Petschek, 1991; Libersky *et al.*, 1993; Liu *et al.*, 2002; Liu *et al.*, 2004]. However, it is computationally less efficient compare to the FEM and suffers from instability problems in certain conditions. Therefore, adopting the SFM, where the SPH method is used at the region of large deformation and damage, and the FEM elsewhere, appears to be a rational choice for high velocity projectile penetration/perforation simulations. Although the SFM is not entirely a new idea, very few attempts have been taken to study the efficiency of the approach.

Failure due to adiabatic shear is common to high strain rate problems of metals [Odeshi *et al.*, 2006]. Taylor and Quinney [1934] mentioned that the work done due to plastic deformation in metal was converted to heat. Dissipation of the heat depends on the thermal diffusion distance which is the distance of heat transfer during a time period, and hence, varies inversely with the strain rate. Thus the heat generated in the specimen by the plastic work remains within the specimen for high strain rates and considered to be an adiabatic condition. However, not all the converted heat remains within the material and a small portion of it is diffused mostly due to radiation and heat conduction. Temperature rise due to the adiabatic condition at high strain rate needs to be included in the material model for metals.

The main objective of this study is to propose a suitable constitutive model for high velocity impact simulations of lightweight structures. The model includes effects of large strain, high strain rate and adiabatic heating condition. Constitutive equations for the model are presented first. Following that, procedure for obtaining material properties of Ti-6Al-4V and AA5083-H116 is described. All the material properties can be identified from uniaxial tests at various strain rates and temperatures. The model is verified through numerical simulations of split Hopkinson pressure bar (SHPB) tests at various temperatures, and finally, adopted to simulate the perforation and/or penetration of Ti-6Al-4V and AA5083-H116 plates.

2. Coupled SPH-FEM (SFM)

Finite element method (FEM) is versatile for solving many physical and engineering problem but suffers from severe mesh distortion problem in high velocity impact

analyses. The smooth particle hydrodynamics (SPH) method is by nature a discrete and mesh free approach and hence suitable for this type of problems that involve severe damages but is less efficient computationally. SPH also inherently suffers from certain instability problems. Though each method has its own certain advantages and disadvantages but when they are combined as the coupled SPH-FEM method (SFM), the approach mitigates fatal FE problems at minimal increase in computational cost. To optimize the computational resources, in the SFM, the SPH particles are employed only in the region of large deformation and damage, while the rest of the domain is modeled by the finite element (FE) mesh. Application of the SPH method mitigates any numerical problems encountered in FE approach because of large deformation, while using the FEM for the rest of the domain improves the accuracy of the results and contains the requirement on computational resources. Compared to either FEM or SPH method for high velocity impact analyses, the SFM performs significantly better with less computational effort.

Both SPH and FE methods are based on the Lagrangian formulation. The SPH method can be easily included in an existing Lagrangian based FEM by considering SPH particles as elements with one node. Schematic overview of the Lagrangian SPH and FEM, as shown in Fig. 1, elaborates the difference between the two methods, determination of strains, strain rate and forces. Same material model and equation of state are applicable for both methods. Therefore, it is possible to combine the two methods with appropriate conditions imposed at the interface.

The interface between elements and particles ensures continuous bonding of the two methods. At the interface, the SPH particles are constrained and moved with the elements. A node to surface contact option is used to link the SPH particles and finite element surfaces where, the SPH particles are considered as slave nodes and the side of the finite element surface is treated as the master surface. Possible penetration of the slave nodes are continuously monitored and mitigated if only throughout the calculation procedure with slave nodes displacements [Attaway *et al.*, 1994]. Figure 2 describes link between the finite elements and SPH particles. The influence sub-domain of the particles at/near the interface zone such as the particle p_1, covers both the FE and SPH particles, and hence certain considerations are required in the computation. For strain and strain rate calculation of each
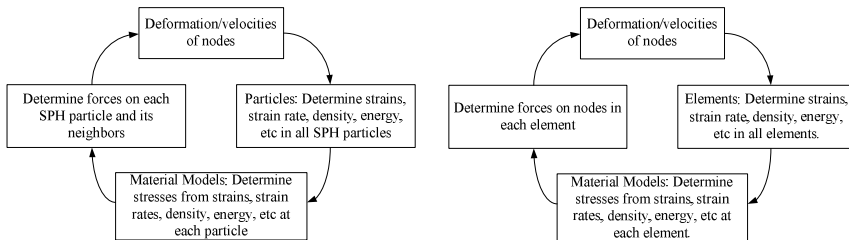

Fig. 1.   Lagrangian code structures for SPH particles and FEM elements.

Interface between FEM and SPH
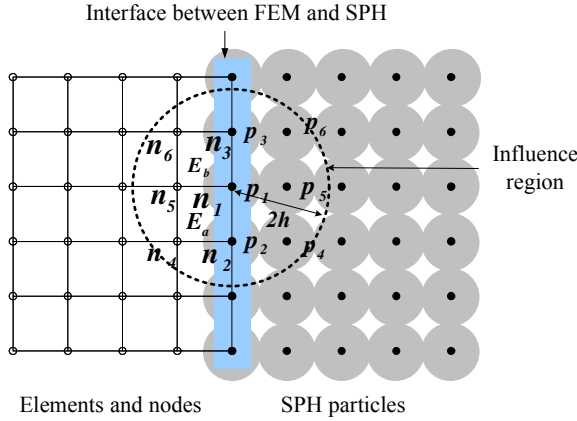

Elements and nodes   SPH particles

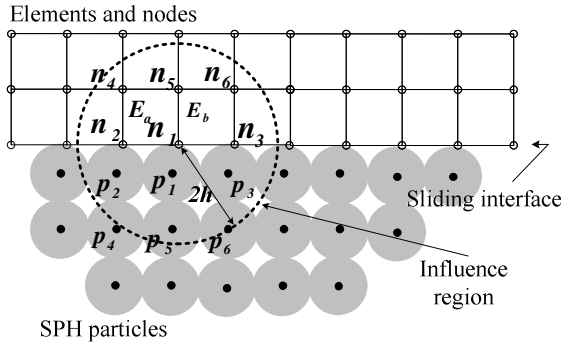Fig. 2. Coupled SPH-FE method: linking between the finite elements and SPH particles.

Fig. 3. Coupled SPH-FE method: sliding between the finite elements and SPH particles.

particle ($\boldsymbol{p}_1$), only the SPH particles inside the influence sub-domain ($\boldsymbol{p}_1, \ldots, \boldsymbol{p}_6$) are considered. However, for force calculation both SPH particles ($\boldsymbol{p}_1, \ldots, \boldsymbol{p}_6$) and interface elements ($\mathbf{E_a}$ and $\mathbf{E_b}$) inside the influence sub-domain are used. Fig. 3 demonstrates the sliding interface between the SPH particles and finite elements. This is particularly significant for penetration events where projectile is modeled using finite elements and the target is consisted of SPH particles. Again a node to surface contact is used where, the SPH particles are considered as slave nodes and the side of the finite element surface is treated as the master surface.

3. Material Model

To model the response of materials under high velocity impact, it is essential to use a robust material model that can incorporate high strain rate, large strain and thermal softening effects along with a reliable fracture modeling. The popular Johnson-Cook

(JC) model [Johnson and Cook, 1983; Johnson and Cook, 1985] incorporates most of the effects except for temperature effects due to adiabatic heating. Therefore, a modified version of the JC model, allowing adiabatic heating, high strain rate and large strain effects, is proposed in this study.

3.1. *Modified Johnson-Cook Model*

Low strain rate is often considered as the isothermal process and high strain rate as the adiabatic process. Fig. 4(a) demonstrates a stress-strain curve for metal where work hardening rate is observed under isothermal conditions. Because work done in plastic flow is converted to heat, in an adiabatic condition material temperature will increase, and gradually reduces the work hardening rate leading to material softening as shown in Fig. 4. Not all the generated heat remains within the specimen. A small portion of it is lost due to radiation and heat conduction. Since adiabatic shear failure is prominent to high velocity impact problems for metals it is necessary to include temperature effect due to adiabatic condition.

The temperature increment due to adiabatic condition can be derived using the following equation,

$$\Delta T = \frac{\beta}{\rho C_p} \int \sigma(\varepsilon_p) d\varepsilon_p \tag{1}$$

where, β is the percentage of work converted to heat, C_p is the specific heat and ρ is the density of the material. The value of β varies from zero with total dissipation of heat (isothermal) to 1 with no loss of heat (adiabatic). Mason *et al.* [1994] measured β value for 2024 aluminum, 4340 steel and Ti-6Al-4V at strain rates of $3000\,\text{s}^{-1}$, $2500\,\text{s}^{-1}$ and $1500\,\text{s}^{-1}$ respectively using the infrared radiometer, and found that the β value varies between 0.5 to 0.95. Kapoor and Netmat-Nasser [1998] and Nemat-Nasser and Kapoor [2001] conducted tests on several materials, namely Ta-2.5% W, titanium, 1018 steel, 6061-T6 aluminum, OFHC copper, and Ti-6Al-4V at high strain rates (2000–$3000\,\text{s}^{-1}$) and concluded that within test error, all the work done was converted to heat, i.e. $\beta = 1.0$. Taylor and Quinney [1934] observed β value around 0.9 from the rapid torsion and compression tests on mild steel and copper.
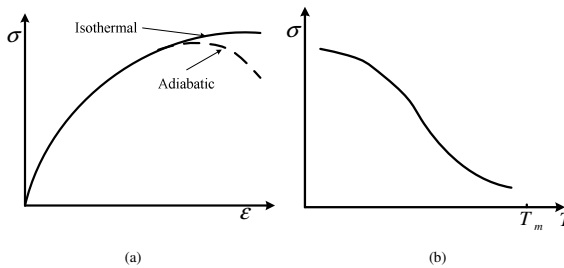

Fig. 4.   (a) Isothermal stress-strain relationship showing thermal softening (dashed line) due to adiabatic conditions. (b) Thermal softening rate and temperature effect on strength.

Considering these, a rational value of $\beta = 0.9$ is used in the proposed model for all the metals.

The strain rate constant, C in the JC model depends on the reference strain rate, $\dot{\varepsilon}_0$. Strain rate expression can also cause mathematical error for $\dot{\varepsilon}_p = 0$. A new strain rate effect expression is proposed for the modified Johnson-Cook (MJC) model, and one additional material constant is reduced. The new expression is much simpler than that of the JC model and determining the strain rate parameter is straightforward.

The equivalent stress, damage and fracture strain of the modified Johnson-Cook (MJC) model are expressed as,

$$\sigma = [A + B(\varepsilon_p)^a][\dot{\varepsilon}_p]^C[1 - ((T - T_r)/(T_m - T_r))^b] \tag{2}$$

$$D = \sum_{t=0}^{t_{cur}} \frac{\Delta \varepsilon_p}{\varepsilon^f} \tag{3}$$

$$\varepsilon^f = (D_1 + D_2 \exp D_3(\sigma_{ave}/\sigma_e))(\dot{\varepsilon}_p)^{D_4}(1 + D_5((T - T_r)/(T_m - T_r))) \tag{4}$$

In Eq. (2), ε_p is the equivalent plastic strain, $\dot{\varepsilon}_p$ is the plastic strain rate, $(\dot{})$ implies differentiation with respect to time, T_m and T_r are the melting and room temperatures respectively, t_{cur} is the time at the current step, σ_{ave} and σ_e are the average of normal stresses and von Mises stress respectively, A, B, a, C and b are the material constants. The three brackets in Eq. (2) take into account the effects of plastic strains, the strain rates and the temperature respectively. Fracture in materials occurs by element erosion when D is unity. D_1 to D_5 in Eq. (4) are the five damage parameters. This damage model is often adopted as a remedial measure for severe element distortion problem in the FE simulation, but it is not included for the SFM simulation in the present study.

3.2. *Procedure for Obtaining MJC Material Model Parameters*

3.2.1. *Material Model Properties for Titanium Alloy*

Determining the material model parameters for the MJC model requires careful consideration and well defined procedures. There are five material parameters required to determine the equivalent stress for the MJC model. The first three parameters (A, B and a) describe the plastic deformation of the material, the fourth parameter C contributes to the strain rate effect, and the last parameter b reflects the temperature effect. Three steps are required to calculate all the parameters for any materials. The procedure of calculating material parameters is described herein using the experimental results from various tests of titanium alloy Ti-6Al-4V conducted by Khan *et al.* [2004] such as (1) quasi-static compression test at room temperature and strain rate of $1\,\mathrm{s}^{-1}$, (2) compression tests at strain rates of $10\text{-}5\,\mathrm{s}^{-1}$, $10\text{-}3\,\mathrm{s}^{-1}$, $1\,\mathrm{s}^{-1}$ and $3378\,\mathrm{s}^{-1}$, and (3) quasi-static tests at strain rate of $0.01\,\mathrm{s}^{-1}$ and temperatures 149°C, 315°C and 482°C.

Step 1: The flow stress of the MJC model is shown in Eq. (2). At room temperature (for example, 25°C) and unit strain rate, Eq. (2) can be expressed as,

$$\sigma = [A + B(\varepsilon_p)^a] \tag{5}$$

A Fortran program is used to determine the material parameters A, B and a using the best fit curve from the experimental stress-strain data at room temperature and unit strain rate, which is found to be 1112.0 MPa, 1082 MPa and 0.686, respectively. Comparison of the experimental and predicted stress-strain plot is illustrated in Fig. 5.

Step 2: The strain rate effect parameter C is determined from the $\sigma - \dot{\varepsilon}_p$ plot. At room temperature, Eq. (2) can be expressed as,

$$\sigma = \sigma_A[\dot{\varepsilon}_p]^C \tag{6}$$

$$\log_{10}(\sigma) = \log_{10}(\sigma_A) + C \log_{10}[\dot{\varepsilon}_p] \tag{7}$$

where, $\sigma_A = [A + B(\varepsilon_p)^a]$. Least square line method is applied to determine the strain rate parameter C. Figure 6 shows the calculated C values at various plastic strains that reach an approximate uniform value of 0.0133 at plastic strain of 0.06 and greater.

Step 3: The temperature effect parameter b is obtained using the $\sigma - T$ plot. For the same set of materials at similar range of strain rate value, Eq. (2) can be written as,
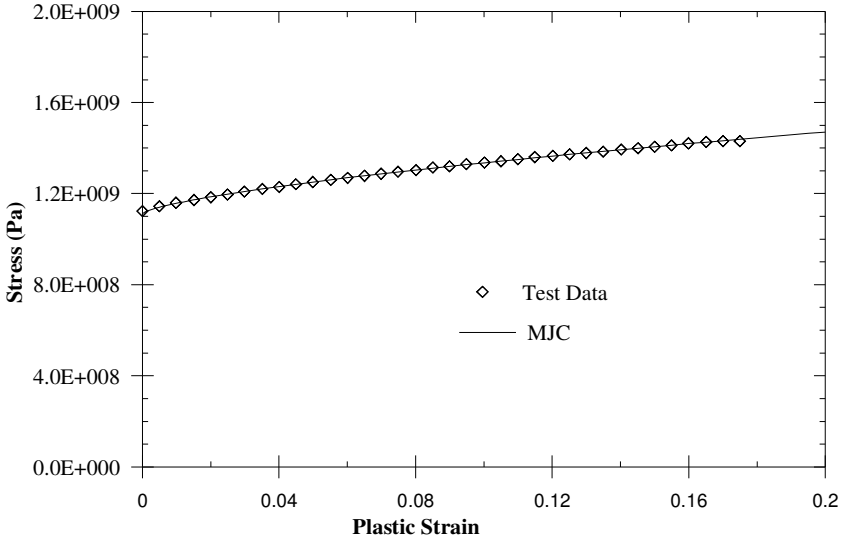

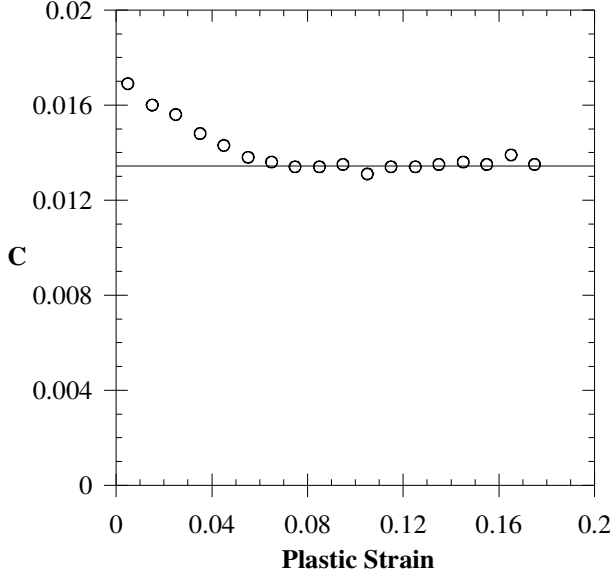Fig. 5.   Stress-plastic strain relationship for Ti-6Al-4V at a strain rate value of $1\,\mathrm{s}^{-1}$.

Fig. 6. Variation of C value for Ti-6Al-4V at various plastic strains.

$$\sigma = \sigma_B[1 - \bar{T}^b] \tag{8}$$

$$\log_{10}\left(1 - \frac{\sigma}{\sigma_B}\right) = b\log_{10}(\bar{T}) \tag{9}$$

$$b = \log_{10}\left(1 - \frac{\sigma}{\sigma_B}\right)/\log_{10}(\bar{T}) \tag{10}$$

where, $\sigma_B = [A + B(\varepsilon_p)^a][\dot{\varepsilon}_p]^C$ which can be calculated using the previously determined parameters for various plastic strains, and $\bar{T} = (T - T_r)/(T_m - T_r)$ is the homogenous temperature. Figure 7 illustrates the variation of parameter for plastic strain ranging from 0.01 to 0.18 at temperatures 149°C, 315°C and 482°C and strain rate of $0.01\,\mathrm{s}^{-1}$. Isothermal condition is assumed at this low strain rate. As shown in Fig. 7, the value of b reaches a steady value of about 0.8 when plastic strain exceeds about 0.04. Ti-6Al-4V alloy has two phases, namely alpha and beta phases and it transforms from alpha phase to beta phase at temperature of 996°C (beta transus temperature). The effects of temperature on material properties change abruptly at the phase transition. The proposed MJC model material parameters are thus applicable only for Ti-6Al-4V at or below beta transus temperature.

Values of the five parameters for Ti-6Al-4V are summarized in Table 1 along with other material properties. Experimental stress-strain plots at various strain rates and temperatures [Khan *et al.*, 2004] are compared with the MJC predicted data in Fig. 8, and indeed, they show reasonably good agreement. The material parameters
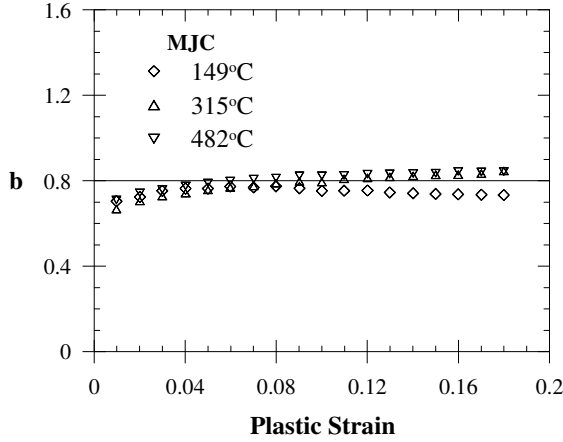
Fig. 7.   Variation of *b* value for Ti-6Al-4V at various plastic strains.

Table 1.   Ti-6Al-4V material parameters for the MJC model.

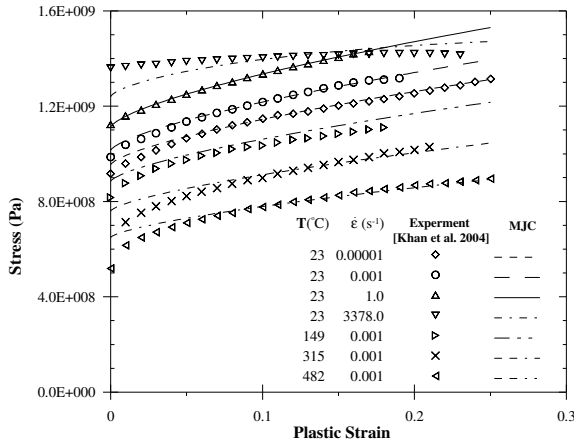| ρ_0 (kg/m^3)	E (GPa)	ν	G (GPa)	A (MPa)	B (MPa)
4450	110.0	0.33	42.5	1112	1082
a	C	b	C_p (J/kgK)	T_m (°K)	T_r (°K)
0.686	0.0133	0.80	560	1877	298

Fig. 8.   Comparison of the MJC model with the experimental data for Ti-6Al-4V.

are validated against two other different material test data of commercial Ti-6Al-4V conducted by Nemat-Nasser *et al.* [2001] and Seo *et al.* [2005]. Figures 9–10 demonstrate the experimental and predicted stress-strain plots. The MJC model exhibits a good correlation with most experimental results.
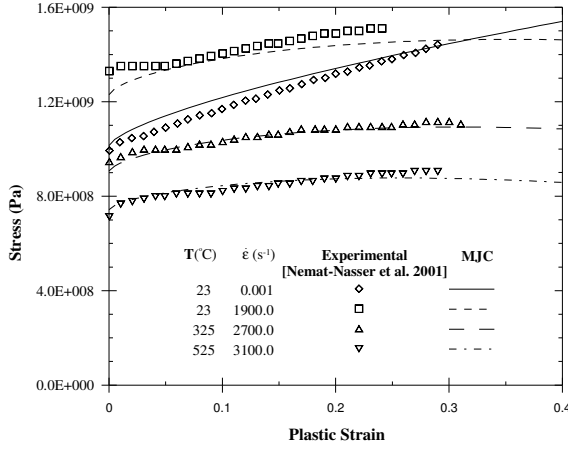
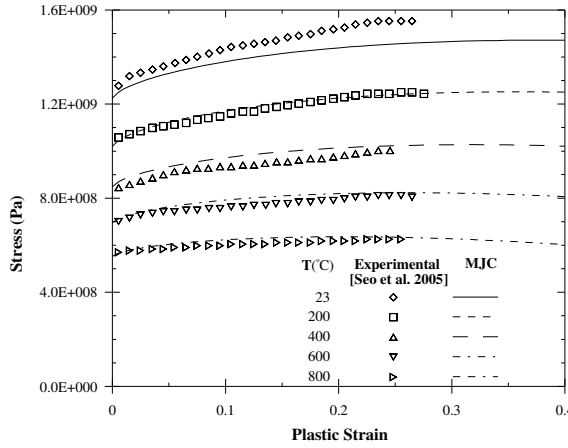Fig. 9.   Comparison of the MJC model and the test data for Ti-6Al-4V.

Fig. 10.   Comparison of the MJC model and the experimental results at strain rate of $1400\,\mathrm{s}^{-1}$ for Ti-6Al-4V.

3.2.2. *Material Model Properties for Aluminum Alloy*

The MJC material model properties of aluminum alloy AA5083-H116 are determined from the tensile tests results performed by Clausen *et al.* [2004] at wide range of temperatures and strain rates. They collected the specimens from an AA5083-H116 plate with $25\,\mathrm{mm}$ thickness. Three different test results, namely (1) quasi-static tensile test at room temperature, (2) tensile tests at strain rates of $3.95\,\mathrm{s}^{-1}$, $122\,\mathrm{s}^{-1}$, and $1313\,\mathrm{s}^{-1}$, and (3) quasi-static tests at strain rate of $0.0017\,\mathrm{s}^{-1}$ and temperatures varying between $200°\mathrm{C}$–$500°\mathrm{C}$ are incorporated for material model

Table 2.   AA5083-H116 material parameters for the MJC model.

ρ_0 (kg/m^3)	E (GPa)	ν	G (GPa)	A (MPa)	B (MPa)
2700	70.0	0.3	27.0	160	677
a	C	b	C_p (J/kgK)	T_m (°K)	T_r (°K)
0.55	0.0114	0.56	910	893	293

parameters calculations. Material properties for AA5083-H116 aluminum plate are listed in Table 2.

3.3. *Verification of the MJC Model*

To verify the MJC model, numerical simulations of split Hopkinson pressure bar (SHPB) test on titanium alloy Ti-6Al-4V at various temperatures [Seo *et al.*, 2005] are performed. Specimen temperature varied from room temperature to 1000°C. To keep the specimen strain rate constant ($1400\,\mathrm{s}^{-1}$), strike bar velocity (v_{sb}) varied along with the specimen temperature. The incident, transmitter and strike bars were made of 20.6375 mm diameter Inconel 718. The incident and transmitter bars were 1500 mm long and the strike bar was 500 mm in length. The titanium alloy Ti-6Al-4V was cylinder in shape with 8 mm diameter and 8 mm length.

Numerical simulations are performed using LS-DYNA [Hallquist, 2006]. Figure 11 depicts the 2D axi-symmetrical FE model of the SHPB simulation. A mesh size of $0.4\,\mathrm{mm} \times 0.4\,\mathrm{mm}$ was used for the specimen. An automatic surface to surface contact is used between various surfaces (e.g. strike bar — incident bar, incident/transmitter bar — specimen). The incident, transmitter and strike bar are assumed to behave like elastic material. Therefore, a simple elastic-plastic material model is adopted for the pressure bars. Material properties of the pressure bars are given in Table 3. The MJC model is used for the titanium alloy Ti-6Al-4V as a user defined material model and the material properties for the model is obtained in Section 3.2 and shown in Table 1. The MJC model is unable to predict the behavior of titanium with temperature greater than beta transus temperature (996°C). Therefore, in this study numerical simulation of SHPB test is considered only for initial specimen temperatures ranging from room temperature (25°C) to 800°C.

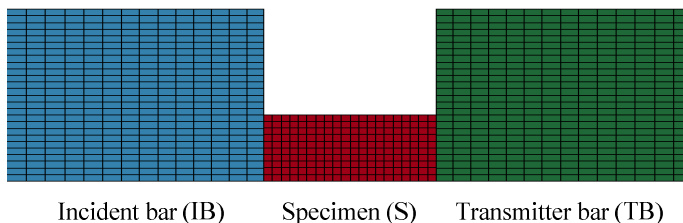Incident bar (IB)   Specimen (S)   Transmitter bar (TB)

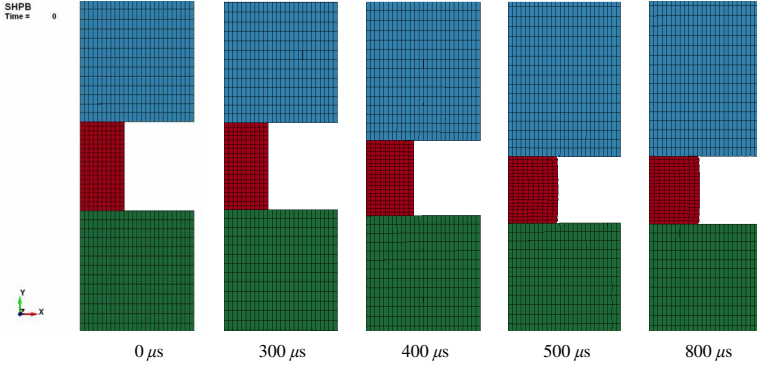Fig. 11.   Numerical model of the Ti-6Al-4V SHPB test.

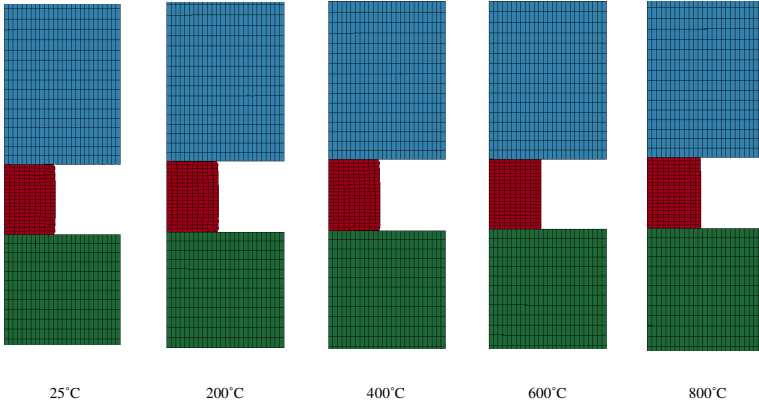Fig. 12. Time history plot of the SHPB test of Ti-6Al-4V specimen at 25°C.

Fig. 13. Deformed Ti-6Al-4V specimens at temperatures ranging from 25°C to 800°C.

Table 3. Material properties for Inconel 718.

σ_Y (GPa)	ρ_0 (kg/m^3)	E (GPa)	ν	E_t (GPa)
1.10	8190	204.9	0.284	1.124

Figure 12 illustrates the deformation of the specimen during the SHPB simulation at various time steps. As shown in the figure, the specimen is subjected to high compressive stress and the final specimen length is around 60% of the original length. Final deformed shapes of the specimen at various temperatures are shown in Fig. 13. Simulated deformed shapes agree well with experimental results reported earlier by Seo *et al.* [2005]. They also measured incident, reflected and transmitted strain voltages at midpoints of the incident and transmitted bars. A conversion factor is used to convert strain voltages to strain (1 volt = 500 microstrain) in this study. Figure 14 compares the experimental and numerical incident,
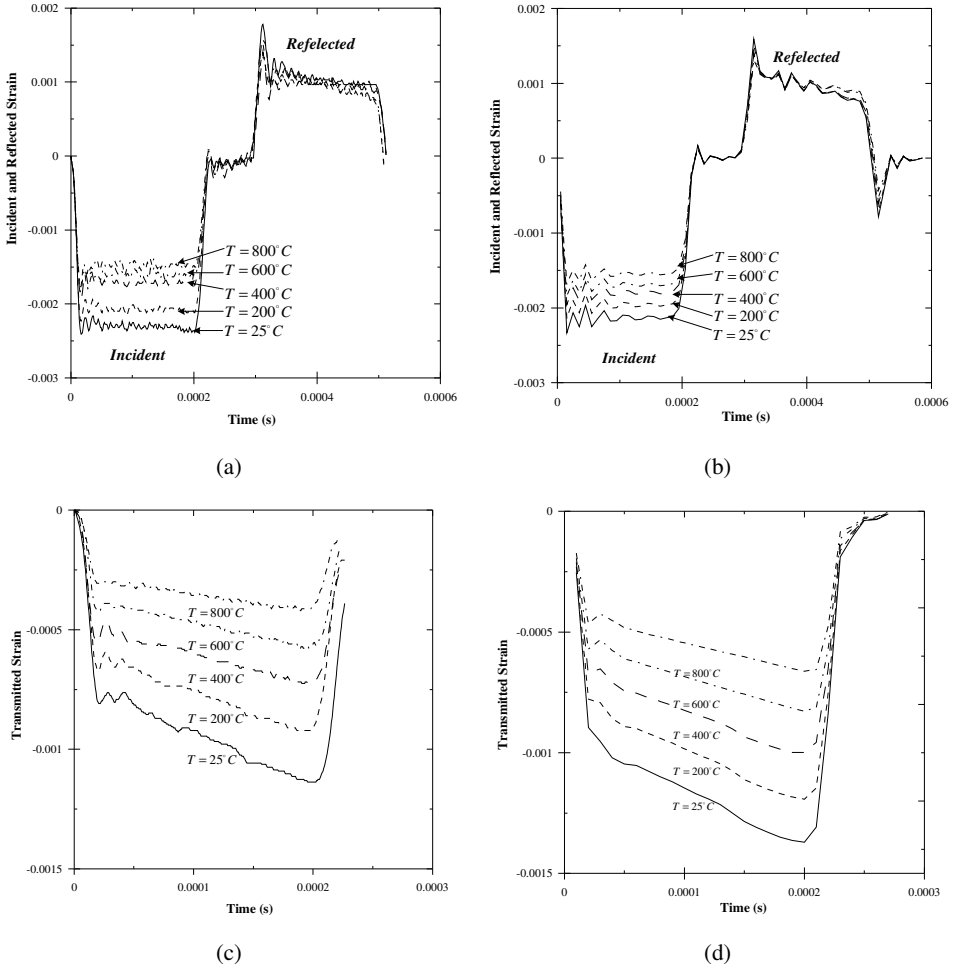
(a)

(b)

(c)

(d)

Fig. 14. Incident, reflected and transmitted strain wave-time histories of the experimental (a, c) and numerical (b, d) SHPB tests of Ti-6Al-4V.

reflected and transmitted strain-time history plots at various temperatures. Simulation results show similar pattern observed in the test. Although magnitude of the strains slightly differs from the test data, it is within the acceptable range.

4. Perforation of Ti-6Al-4V Plate Using MJC Model

Burkins *et al.* [2001] published ballistic test results of 26.72 mm thick titanium alloy Ti-6Al-4V target plate. The fragment-simulating projectile (FSP) with 20 mm diameter was used as the projectile. Geometry and dimensions of the FSP are demonstrated in Fig. 15. Several penetration and/or perforation studies were conducted with impact velocities ranging between 950–1060 m/s. The experimental
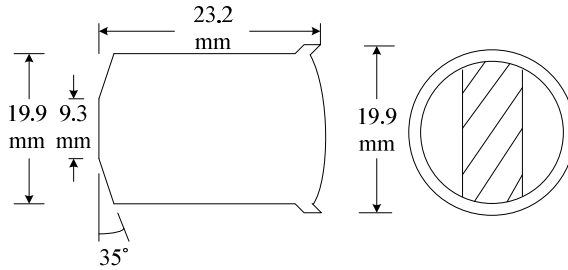
Fig. 15.   Geometries and dimensions of the 20 mm fragment-simulating projectile (FSP).

ballistic limit velocity of the 26.72 mm plate is 1023 m/s with a standard deviation of 13 m/s. The present study involves the SFM simulation of the perforation of Ti-6Al-4V plate using the MJC model for target material.

4.1. *Material Properties of MIL-T-9046J Ti-6Al-4V*

Target plates are made of titanium alloy Ti-6Al-4V with aerospace specification MIL-T-9046J, and have yield and ultimate tensile strengths of 875.6 MPa and 972.2 MPa respectively with 15% of elongation [Burkins *et al.*, 2001]. Based on these mechanical properties, strength material parameters (A, B and a) for the MJC model are determined first. However, lack of strain rate information for the tensile tests makes it difficult to predict accurate strength parameters. Quasi-static tensile tests of specimens can be performed using a MTS servo hydraulic testing machine at strain rates between $10^{-5} - 10^2 \mathrm{s}^{-1}$. Therefore, three strain rate cases such as, low, moderate and high strain rates (AL $= 10^{-4}\,\mathrm{s}^{-1}$, AM $= 1\mathrm{s}^{-1}$ and AU $= 10^2\,\mathrm{s}^{-1}$) are considered to determine the strength parameters. Least square method is applied to determine the parameters, and indeed, Table 4 gives all the parameters for various cases. As observed in the Table 4, strength parameters vary with the choice of strain rate case. For example, low and high strain cases give higher and lower material strength, respectively. This is due to the fact that strength parameters are determined for strain rate value of $1\,\mathrm{s}^{-1}$, and will give higher values when yield strength is determined for strain rate value less than $1\,\mathrm{s}^{-1}$ and vice versa. Other material parameters are believed to be similar to the commercial Ti-6Al-4V and are already determined in Section 3.2. Table 5 summarizes other material properties.

Table 4. MJC strength material parameters for 26.72 mm thick MIL-T-9046J Ti-6Al-4V plate.

Case	AL	AM	AU
A (MPa)	976.0	863.0	811.0
B (MPa)	447.0	396.0	376.0
A	0.686	0.686	0.686

Table 5.   MJC material properties for titanium alloy Ti-6Al-4V plate.

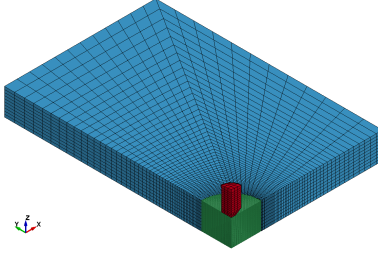| ρ_0 (kg/m^3)	E (GPa)	ν	G (GPa)	C	b	C_p (J/kgK)	T_m (°K)	T_r (°K)
4430	99.2	0.33	37.3	0.0133	0.80	560	1877	296

Fig. 16.   Target and FSP projectile numerical model for Ti-6Al-4V plate perforation.

4.2. *Ballistic Numerical Simulation Using Coupled SPH-FEM (SFM)*

In the experiment, multiple perforation tests were performed with a single 305 mm × 457 mm target plate. However, in the simulation only one impact test is conducted at the middle of the target plate. The target plates and projectiles are modeled using the SFM and FEM respectively. Figure 16 describes the numerical model of the projectile and target plate. Selection of SPH domain size is important for the SFM. Swaddiwudhipong *et al.* [2010] studied the effect of SPH domain radius and decided on an optimum SPH domain radius of 2 to 3 times projectile radius. In this study, SPH particles are utilized at the middle of the target plate with a larger SPH domain radius of 30 mm in order to limit the exit surface bulge within the SPH domain. Because of the high impact velocity and non-regular projectile shape, the area of the exit surface bulge is larger than those of the earlier studies. Swaddiwudhipong *et al.* [2010] also performed initial SPH particle distance study and selected particle distance of 0.6 mm for steel and aluminum plate perforation. The initial SPH particle distance of 0.8 mm is used for Ti-6Al-4V plate perforation since the particle distance of 0.6 mm has shown some unexplained instability during the simulations. For the FEM, 8 node solid elements are adopted. Only a quarter of the problem is modeled using symmetry in *xz* and *yz* planes. The projectile is made of 4340H steel and the material properties are given in Table 6. The projectile is modeled using an elastic/plastic material model with isotropic hardening. In the simulation, the projectile impact velocities varied between 1000–1300 m/s.

Table 6.   Material properties for 4340H steel.

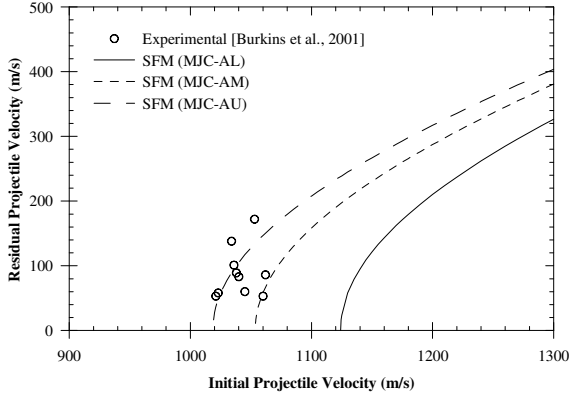| σ_Y (GPa)	ρ_0 (kg/m^3)	E (GPa)	ν
0.435	7850	205.0	0.29

Fig. 17. Numerical and experimental residual velocities of FSP perforating Ti-6Al-4V plates.

Ti-6Al-4V titanium alloy has high strength but relatively low thermal conductivity. Because of these characteristics, during the high velocity penetration event target material melt [Woodward, 1979] at the projectile-target interface, which significantly reduces the frictional effect between the projectile and target. Therefore, no friction is included for Ti-6Al-4V perforation.

4.3. *Residual Velocity Comparison*

Residual velocities for three cases are measured from the numerical simulation and plotted in Fig. 17 along with the experimental data. The numerical initial and residual velocities are plotted using an analytical model originally developed by Recht and Ipson [1963].

$$v_r = o(v_i^q - v_{bl}^q)^{1/q} \tag{11}$$

where, v_i, v_r and v_{bl} are initial, residual and ballistic limit velocities respectively, o and q are the model constants which can be determined using the least square method. The numerical ballistic limit velocities for AL, AM and AU cases are 1124.0, 1053.5 and 1018.5 m/s respectively. The model constants o and q are calculated with v_i, v_r and v_{bl}, and are found to be 0.5 and 2 respectively for all three cases.

Low strain rate case, AL underestimates the residual velocities and overestimates the ballistic limit velocity compared to the experimental results. Although AU case seems to show better agreement with the experimental observation, it is difficult to achieve strain rate of $10^2\,\mathrm{s}^{-1}$ in a MTS servo hydraulic machine. Moderate strain rate case, AM provides most rational material properties, and the ballistic limit velocity of 1053.5 m/s correlates well with the experimental ballistic limit velocity of 1023 m/s.

The FSP geometry is different from those of other projectiles discussed earlier including projectiles with blunt, ogival and conical noses. Therefore, failure patterns
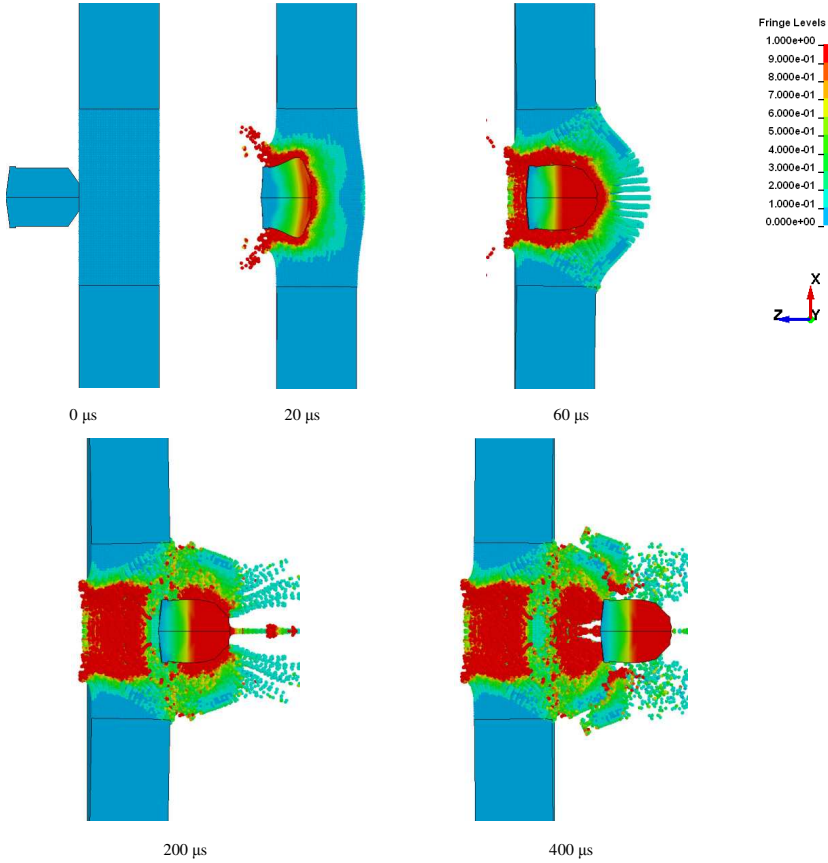
Fig. 18.   Time history of 26.72 mm thick Ti-6Al-4V plate perforated by FSP at $v_i = 1060 \, \text{m/s}$ with effective plastic strain fringe contour.

of the target plates due to the former are different, as expected from those of the latter. A combination of failure patterns such as, ductile hole enlargement, adiabatic shear band and fractures due to bending is observed in Ti-6Al-4V perforation simulations. Figure 18 demonstrates the perforation process of the FSP with 1060 m/s initial impact velocity. Due to the blunt tip of the projectile, a sharp indentation is observed initially with significant projectile deformation. At this stage, failure occurs within a narrow localized zone due to shear bands around the projectile periphery. The next step shows a change in the projectile nose to that of a hemispherical shape and the projectile progresses through the target plate by moving the materials in radial direction. The target plate is subjected to bulging and thinning at the rear surface which causes intensive tensile strain zone. Fracture appears when tensile strain exceeds material capacity and petals are formed. Separation of petals is also observed and because of that a larger exit crater than the entry crater is detected.

Table 7.   Material properties for Hardened Arne tool-steel [Dey, 2004].

σ_Y (GPa)	ρ_0 (kg/m^3)	E (GPa)	ν	E_t (GPa)
1.90	7850	204.0	0.33	15.0

5. Perforation of Aluminum Plate Using MJC Model

Aluminum-magnesium alloy AA5083-H116 is a lightweight material with high strength, and hence, widely adopted for aerospace and military structures. Børvik *et al.* [2004] performed perforation of 25 mm thick AA5083-H116 target plate by conical nose steel projectile with initial strike velocity ranging between 250–360 m/s. In the numerical simulations, the SFM is used for the target plate where the SPH particles are employed at the center of the plate. A SPH domain radius of 24 mm and the initial SPH particle distance of 0.6 mm are implemented in this study [Swaddiwudhipong *et al.*, 2010]. The projectile is modeled using 8 node solid elements in the FEM. Quarter of the problem domain is considered for the simulations using symmetry in two planes. The projectile is made of Hardened Arne tool-steel and the material properties are shown in Table 7. An elastic/plastic material model with isotropic hardening is incorporated for the projectile since damage in the projectile is negligible. Initial impact velocities of the projectile vary between 250 m/s to 400 m/s. Considering the friction effect between the projectile and target for relatively low projectile velocities, a friction value of 0.02 is incorporated for the aluminum plate perforation simulations [Swaddiwudhipong *et al.*, 2010].

The MJC model is adopted for the AA5083-H116 target plate in the numerical simulations. Material properties of the target material is listed in Table 2. Figure 19 compares the experimental and numerical residual velocities for different strike velocities. Numerical results using the MJC model show good correlation with the experimental results. Compare to the experimental ballistic limit velocity of 256.6 m/s, a ballistic limit velocity of 258 m/s is achieved numerically.
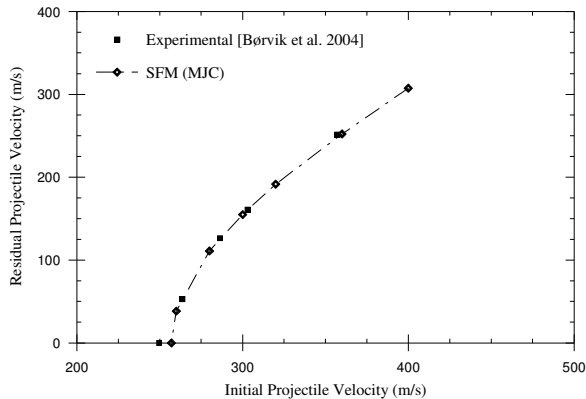

Fig. 19.   Numerical and experimental residual velocities for 25 mm thick AA5083-H116 plates.

6. Conclusions

The MJC model for metals includes strain rate and temperature effects especially at adiabatic conditions. Procedure for obtaining the MJC model parameters is straightforward and the values can be determined from uniaxial tests at various strain rates and temperatures. The proposed model is adopted through user defined material model and simulation results are verified against the test observations. Numerical simulations of SHPB tests of Ti-6Al-4V at various temperatures and high strain rate show good agreement with the experimental results. Finite element analysis using the MJC model is able to predict the final deformed shapes of the specimens at various temperatures. Comparison of the incident, reflected and transmitted strain histories show similar patterns for both numerical and experimental cases.

Perforation simulations of 26.72 mm thick Ti-6Al-4V and 25 mm thick AA5083-H116 target plates are performed using the MJC model for the target plates. Severe element distortion problems for high velocity impact problems are avoided by adopting the SFM. Good correlations between the experimental and numerical residual and ballistic limit velocities are accomplished for both materials. Ballistic limit velocities of 1053.5 m/s and 258 m/s are achieved numerically which are in good agreement with that of 1023 m/s and 256.6 m/s obtained experimentally for Ti-6Al-4V and AA5083-H116 target plates, respectively. Numerical simulations also provide detailed failure patterns of the target plates. It is further shown that the exit target surface for Ti-6Al-4V is subjected more damage and deformation compare to the entry surface, which is consistent with the experimental assessment.

References

Attaway, S. W., Heinstein, M. W. and Swegle, J. W. [1994] "Coupling of smooth particle hydrodynamics with the finite element method," *Nuclear Engineering and Design* **150**(2–3), 199–205.

Børvik, T., Clausen, A. H., Hopperstad, O. S. and Langseth, M. [2004] "Perforation of AA5083-H116 aluminium plates with conical-nose steel projectiles–experimental study," *International Journal of Impact Engineering* **30**(4), 367–384.

Burkins, M. S., Paige, J. I. and Hansen, J. S. [1996] "A ballistic evaluation of Ti-6Al-4v vs. long rod penetrators," U.S. Army Research Laboratory, Aberdeen Proving Ground, MD 21005–5066.

Burkins, M. S., Wells, M., Fanning, J. and Roopchand, B. [2001] "The mechanical and ballistic properties of an electron beam single melt of Ti-6Al-4V plate," U.S. Army Research Laboratory, Aberdeen Proving Ground, MD 21005–5066.

Clausen, A. H., Børvik, T., Hopperstad, O. S. and Benallal, A. [2004] "Flow and fracture characteristics of aluminium alloy AA5083-H116 as function of strain rate, temperature and triaxiality," *Materials Science and Engineering A* 364(1–2), 260–272.

Gingold, R. A. and Monaghan, J. J. [1977] "Smoothed particle hydrodynamics — Theory and application to non-spherical stars," *Royal Astronomical Society, Monthly Notices* **181**, 375–389.

Hallquist, J. O. [2006] "LS-DYNA Theory Manual," Livermore Software Technology Corporation, Livermore, California, USA.

Hatch, J. E. [1984] *Aluminum: Properties and Physical Metallurgy* (Aluminum Association Inc. and ASM International.

Johnson, G. R. [1977] "High velocity impact calculations in three dimensions," *Journal of Applied Mechanics, Transactions ASME*, **44**(1), 95–100.

Johnson, G. R. and Cook, W. H. [1983] "A constitutive model and data for metals subjected to large strains, high strain rates and high temperatures," *7th International Symposium on Ballistics*, The Hague, The Netherlands, pp. 541–547.

Johnson, G. R. and Cook, W. H. [1985] "Fracture characteristics of three metals subjected to various strains, strain rates, temperatures and pressures," *Engineering Fracture Mechanics* **21**(1), 31–48.

Kapoor, R. and Nemat-Nasser, S. [1998] "Determination of temperature rise during high strain rate deformation," *Mechanics of Materials* **27**(1), 1–12.

Khan, A. S., Suh, Y. S. and Kazmi, R. [2004] "Quasi-static and dynamic loading responses and constitutive modeling of titanium alloys," *International Journal of Plasticity* **20**(12), 2233–2248.

Libersky, L. D. and Petschek, A. G. [1991] "Smooth particle hydrodynamics with strength of materials," in *Advances in the Free-Lagrange Method Including Contributions on Adaptive Gridding and the Smooth Particle Hydrodynamics Method: Proceedings of the Next Free-Lagrange Conference Held at Jackson Lake Lodge, Moran, WY, USA 3–7 June 1990*, ed. H. E. Trease, M. F. Fritts and W. P. Crowley (edn. Springer Berlin/ Heidelberg, pp. 248–257.

Libersky, L. D., Petschek, A. G., Carney, T. C., Hipp, J. R. and Allahdadi, F. A., [1993] "High strain Lagrangian hydrodynamics: A three-dimensional SPH code for dynamic material response," *Journal of Computational Physics* **109**(1), 67–75.

Liu Z. S. and Swaddiwudhipong S. [1997] "Dynamic Response of Plate and Shell Structures under Low Velocity Impact," *Journal of Engineering Mechanics ASCE*, **123**(12), 1230–1237.

Liu, Z. S., Swaddiwudhipong, S. and Koh, C. G. [2002] "Stress wave propagation in 1-D and 2-D media using smooth particle hydrodynamics method," *Structural Engineering and Mechanics* **14**(4), 455–472.

Liu, Z. S., Swaddiwudhipong, S. and Koh, C. G. [2004] "High velocity impact dynamic response of structures using SPH method," *International Journal of Computational Engineering Science* **5**(2), 315–326.

Liu, Z. S., Lee, H. P. and Lu, C. [2005] "Structural Intensity Study of Plates under Low Velocity Impact," *International Journal of Impact Engineering* **31**(8), 957–975.

Lucy, L. B. [1977] "A numerical approach to the testing of the fission hypothesis," *Astronomical Journal* **82**, 1013–1024.

Mason, J. J., Rosakis, A. J. and Ravichandran, G. [1994] "On the strain and strain rate dependence of the fraction of plastic work converted to heat: An experimental study using high speed infrared detectors and the Kolsky bar," *Mechanics of Materials* **17**(2–3), 135–145.

Montgomery, J. S. and Wells, M. G. H. [2001] "Titanium armor applications in combat vehicles," *JOM Journal of the Minerals, Metals and Materials Society* **53**(4), 29–32.

Nemat-Nasser, S., Guo, W.-G., Nesterenko, V. F., Indrakanti, S. S. and Gu, Y.-B., [2001] "Dynamic response of conventional and hot isostatically pressed Ti-6Al-4V alloys: Experiments and modeling," *Mechanics of Materials* **33**(8), 425–439.

Nemat-Nasser, S. and Kapoor, R. [2001] "Deformation behavior of tantalum and a tantalum tungsten alloy," *International Journal of Plasticity* **17**(10), 1351–1366.

Odeshi, A. G., Al-ameeri, S., Mirfakhraei, S., Yazdani, F. and Bassim, M. N., [2006] "Deformation and failure mechanism in AISI 4340 steel under ballistic impact," *Theoretical and Applied Fracture Mechanics* **45**(1), 18–24.

Recht, R. F. and Ipson, T. W. [1963] "Ballistic perforation dynamics," *Journal of Applied Mechanics* **30**, 384–390.

Seo, S., Min, O. and Yang, H. [2005] "Constitutive equation for Ti-6Al-4V at high temperatures measured using the SHPB technique," *International Journal of Impact Engineering* **31**(6), 735–754.

Swaddiwudhipong S. and Liu Z. S. [1996] "Dynamic response of large strain Elasto-Plastic Plate and Shell Structures," *Thin-Walled Structures* **26**(4), 223–239.

Swaddiwudhipong S. and Liu Z. S. [1997] "Response of laminated composite plate and shell," *Composite Structures* **37**(1), 21–32.

Swaddiwudhipong, S., Islam, M. J. and Liu, Z. S. [2010] "High velocity pentration/perforation using coupled smooth particle hydrodynamics-finite element method," *International Journal of Protective Structures* **1**(4), 489–506.

Taylor, G. I. and Quinney, H. [1934] "The latent energy remaining in a metal after cold working," *Proceedings of the Royal Society Series A* **143**, 307–326.

Woodward, R. L. [1979] "Metallographic features associated with the penetration of titanium alloy targets," *Metallurgical and Materials Transactions A* **10**(5), 569–573.